Theses and Dissertations

Theses, Dissertations, and Senior Projects

January 2019

# Synthesis And Characterization Of Quasi-Two-Dimensional Chromium Sulfides

Furkan Muhammet Altincicek

Follow this and additional works at: https://commons.und.edu/theses

SYNTHESIS AND CHARACTERIZATION OF
QUASI-TWO-DIMENSIONAL CHROMIUM SULFIDES

by

Furkan Muhammet Altincicek

Bachelor of Science, Bilkent University, 2017

A Thesis

Submitted to the Graduate Faculty

of the

University of North Dakota

in partial fulfillment of the requirements

for the degree of

Master of Science
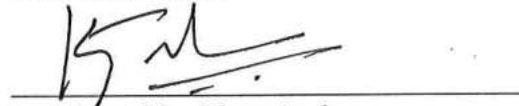
Grand Forks, North Dakota

May

2019

This thesis, submitted by Furkan Muhammet Altincicek in partial fulfillment of the requirements for the Degree of Master of Science from the University of North Dakota, has been read by the Faculty Advisory Committee under whom the work has been done and is hereby approved.

_____
Dr. Nuri Oncel

_____
Dr. Deniz Cakir

_____
Dr. Kanishka Marasinghe

This thesis is being submitted by the appointed advisory committee as having met all of the requirements of the School of Graduate Studies at the University of North Dakota and is hereby approved.

_____
Dr. Chris Nelson, Associate Dean
School of Graduate Studies

_____
4/29/19
Date

# PERMISSION

Title          Synthesis and Characterization of Quasi-Two-Dimensional
Chromium Sulfides

Department    Physics & Astrophysics

Degree         Master of Science

In presenting this thesis in partial fulfillment of the requirements for a graduate degree from the University of North Dakota, I agree that the library of this University shall make it freely available for inspection. I further agree that permission for extensive copying for scholarly purposes may be granted by the professor who supervised my thesis work or, in his absence, by the chairperson of the department or the dean of the School of Graduate Studies. It is understood that any copying or publication or other use of this thesis or part thereof for financial gain shall not be allowed without my written permission. It is also understood that due recognition shall be given to me and to the University of North Dakota in any scholarly use which may be made of any material in my thesis.

<div align="right">

Furkan Muhammet Altincicek
April 11, 2019

</div>

# TABLE OF CONTENTS

# LIST OF FIGURES

# LIST OF TABLES

# ACKNOWLEDGMENTS

I would like to thank my advisor Dr. Nuri Oncel for advising and teaching me for the last two years. Thanks to him, I stepped into the vast world of experimental condensed matter physics. In his labs, I learned and gained my first experiences on the ultra high vacuum systems and other lab techniques. I would also like to thank my committee members Dr. Kanishka Marasinghe and Dr. Deniz Cakir for their help, as well as Dr. William Schwalm and Dr. Yen Lee Loh for teaching me graduate level courses and their help outside the class.

I would like to thank fellow graduate students for their friendship and helpful discussions, especially, Sameera Pathirana for being a very nice roommate for two years and teaching me a whole new culture. I thank my kind neighbor Aliakbar Sepehri for his friendship and his help in physics courses we studied together. I would like to thank Dennis Sisk as well for helping me with the manuscript of this thesis.

Last but not least, I would like to thank my everloving family members, my mother Aydanur Altınçiçek, my father Cahit Altınçiçek and my older brother Ahmet İhsan Altınçiçek for their constant support throughout my life. I would not have succeeded without them.

*Dedicated to my grandfather Emir Deniz,*
*to loving memory of my grandmother Leman Deniz,*
*to my parents Aydanur and Cahit Altincicek,*
*and my aunt Hulya Deniz.*

*Dedem Emir Deniz, rahmetli anneannem Leman Deniz,*
*annem ve babam; Aydanur ve Cahit Altınçiçek*
*ve teyzem Hülya Deniz'e adanmistir.*

# ABSTRACT

Transition metal dichalcogenides (TMDs) are atomically thin semiconductors of the type $MX_2$ with M being a transition metal and X being a chalcogen atom. TMDs have recently attracted considerable attention because of their novel electronic and optical properties. Many TMDs have been studied except $CrS_2$ because of the challenges in its synthesis. However, the most stable form of chromium sulfides, $Cr_2S_3$, chromium (III) sulfide, has been known to exhibit novel properties. For this reason, we studied the possibility of synthesizing thin $Cr_2S_3$ to mimic $CrS_2$. We synthesized single phase $Cr_2S_3$ in vacuum sealed quartz tubes. The synthesis takes about 5 days. After the synthesis, we deposited $Cr_2S_3$ on sapphire substrates via solid-vapor growth method. For characterization, x-ray photoelectron spectroscopy (XPS) and x-ray powder diffraction (XRD) techniques were used and atomic force microscopy (AFM) was used for imaging the quasi-two-dimensional $Cr_2S_3$ particles.

# CHAPTER I

# INTRODUCTION

## 1.1 Motivation

With the discovery of first two-dimensional (2D) material, graphene (honeycomb patterned carbon monolayer), in 2004, interest in similar materials have grown rapidly [1]. The reason for that is graphene and the other discovered 2D materials showed interesting physical, electronic, and optical properties that can be utilized in various areas of applications. These materials are flexible and transparent due to their atomically thin structure and can be metallic, semiconductor, superconductor, or insulator [2].
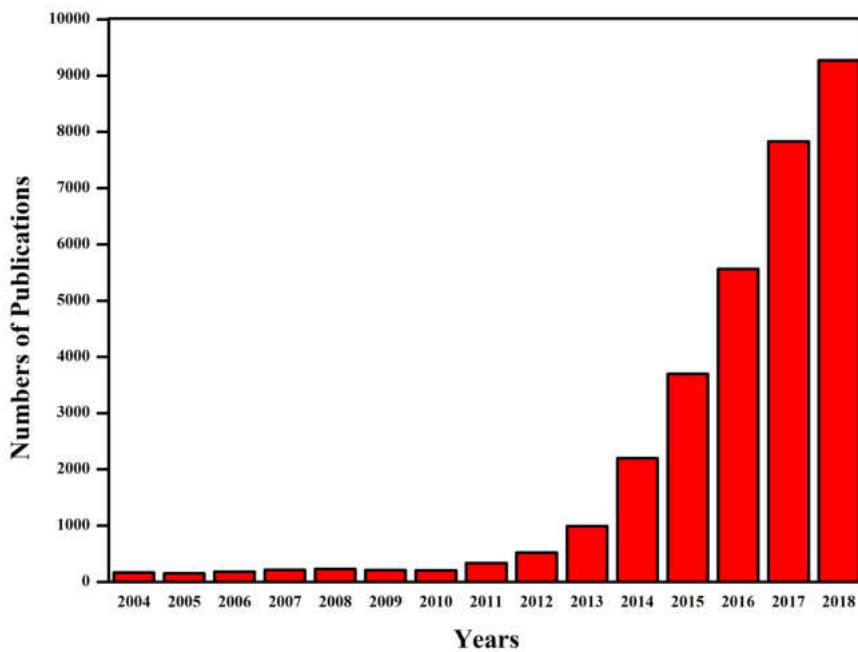
Figure 1: Number of published papers about "Transition Metal Dichalcogenides" by years. Data taken from scholar.google.com.

After graphene, discoveries of various transition metal dichalcogenides (TMD) followed. These are molecules that are composed of one transition metal atom (elements that are partially filled in $d$ orbital or in groups 3-12 in the periodic table) and two chalcogen atoms (elements in group 16 in the periodic table). Simply, one layer of transition metal atoms is sandwiched between two layers of the chalcogen atoms.
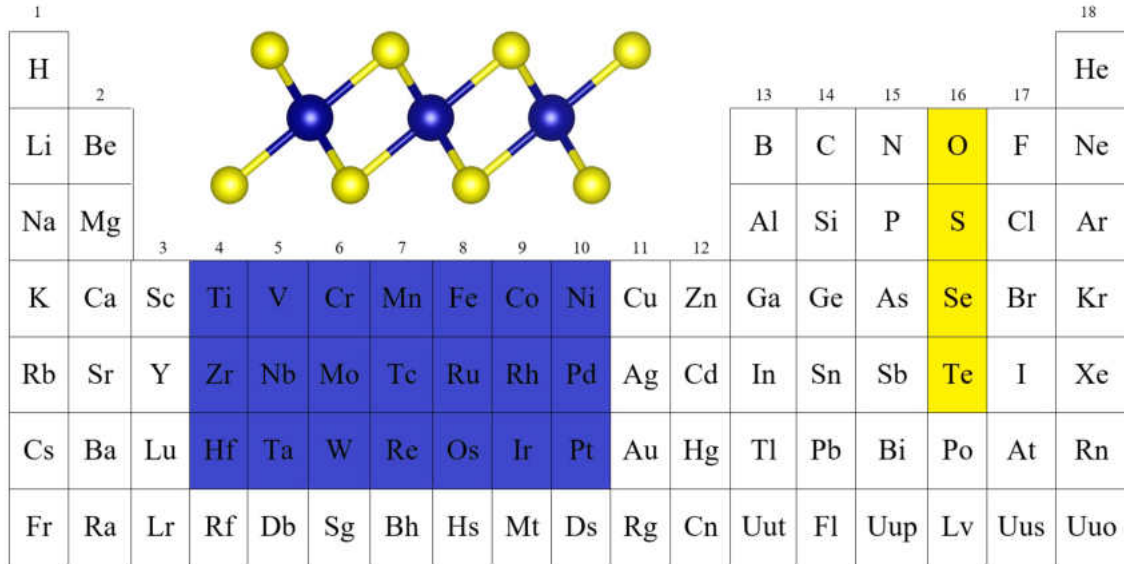


Figure 2: Some transition metals (blue) and chalcogens (yellow) in the periodic table and the sandwich structure of monolayer transition metal dichalcogenides from side view.

This structure allows materials to be atomically thin and that is why they are called two dimensional. Many TMDs show different properties when they are in monolayers than when they are in bulks. Due to their tunable bandgaps and high photoluminescence, it has been reported many times that they have high electron mobility, current on/off ratio and photon absorption which are making them efficient in electronic and optoelectronic applications such as energy storage, various sensors, photonics, circuits, and biomedical devices [2].
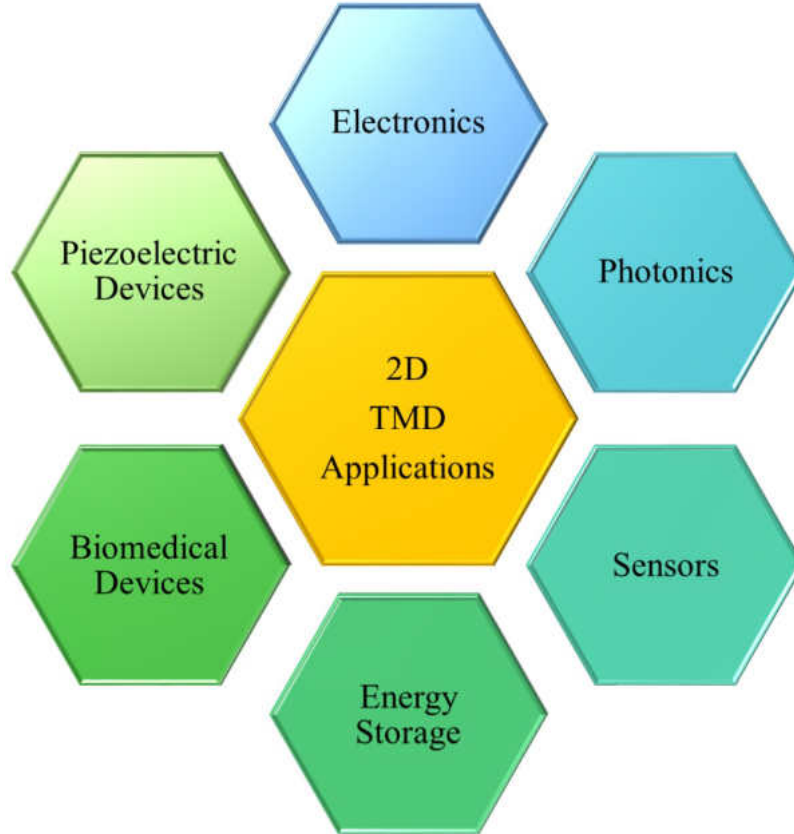
Figure 3: Application areas of 2D TMDs.

## 1.2 Chromium Sulfides

Motivated with the afore mentioned reasons, chromium (IV) sulfide ($CrS_2$) was chosen to be studied. In which case the transition metal is chromium and the chalcogen is sulfur. Expecting chromium to be $+4$ cation and sulfur to be $-2$ anion, they would form $CrS_2$ which would be a TMD. The plan was to synthesize the TMD, characterize and obtain images via a probe microscope. Thus, a literature survey was done on chromium sulfides.

There are plenty of studies in literature about chromium sulfides, in which the big portion of it is based on Jellinek's research, where they studied different compounds and phases of chromium sulfides, their structures and magnetic properties [3]. Nonetheless, none of these studies were about the 2D nature of chromium sul-

fides or about imaging them. Moreover, it was reported in Jellinek's paper that the most common way to synthesize different phases of chromium sulfides would never yield $CrS_2$ nor a pure single phase [3]. Hence, the main interest of the project was shifted to other chromium sulfides, i.e., $Cr_2S_3$ and $Cr_3S_4$, which can exist in either one of two phases; trigonal or rhombohedral. Due to its structure, rhombohedral phase can be grown as quasi-two-dimensional (Q2D). For which a growth method for a single phase is described in another study [4]. Crystal structure of $Cr_2S_3$ is given in Figure 4 generated according to the parameters that are results of computational results reported at materialsproject.org [5]. According to the reported calculations, the rhombohedral $Cr_2S_3$ has the $R\bar{3}$ symmetry and the parameters for its unit cell are; a = b = 0.59 nm and c = 1.6 nm, which will come in handy later when the number of the layers will be calculated. Hence, the goal of the project is changed to synthesize a single phase Q2D $Cr_2S_3$ and its characterization and imaging.
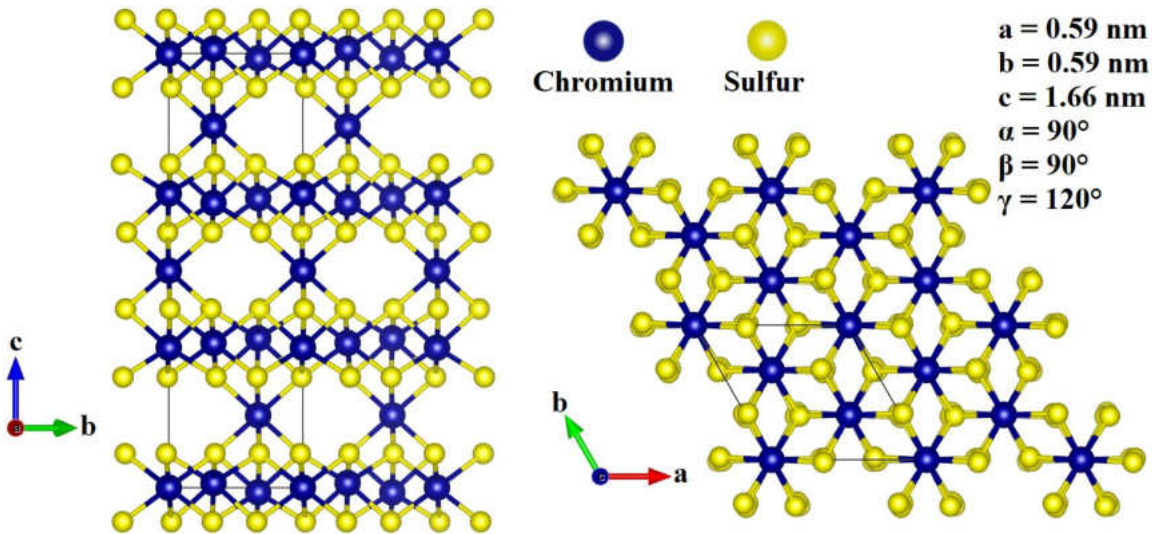


Figure 4: Side and top view of $Cr_2S_3$ respectively.

# CHAPTER II

# METHODOLOGY

## 2.1  Synthesis

### 2.1.1  Equipment

In order to synthesize chromium sulfides, stochiometric ratio of chromium and sulfur powders were planned to be well mixed and then heated at high temperature. For this purpose, high temperature resistant porcelain boat, fused quartz tube, and a tube furnace were used. We used 7 mL combustion boat purchased from Sigma-Aldrich. These porcelain boats, that can resist $1300\,°C$ in vacuum, have dimensions of 10 mm $×$ 97 mm $×$ 16 mm; height, length and width, respectively, and can fit well inside 30 mm diameter fused quartz tubes which can resist $1800\,°C$. For all the reactions described below, we used Lindberg tube furnace that can heat up to $1400\,°C$. Furnace and a tube placed inside it is shown in Figure 5.
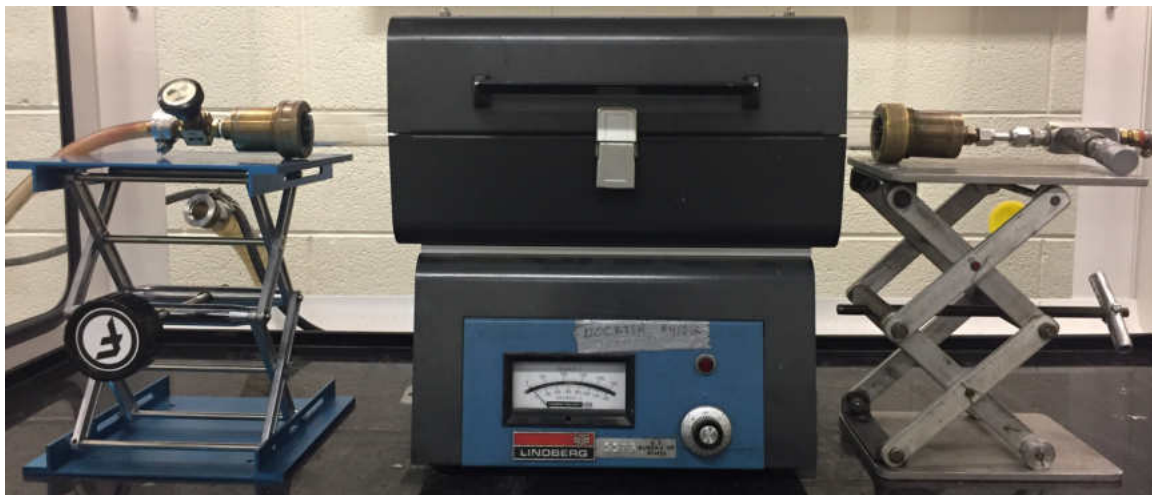


Figure 5: Fused quartz tube inside the furnace.

## 2.1.2  Procedure

We followed the method described in a paper published in 2001 [4]. Firstly, appropriate mixture of 99.5% pure chromium and 99.9% pure sulfur powders (both were bought from Sigma-Aldrich) were mixed, i.e., 1040 mg of Cr and 960 mg of S. With these weights, 0.01 moles of $Cr_2S_3$ was planned to be synthesized. The reaction is as follows:

$$2Cr + 3/8S_8 \rightarrow Cr_2S_3 \tag{2.1}$$

The mixture was put in a ceramic boat which was positioned at the center of a fused quartz tube. On one end of the tube, a clean sapphire sample (1 cm $\times$ 1 cm) was placed. Sapphire samples were used as substrates to deposit the synthesized material. The end, where the sapphire substrate is located, is connected to a pump system (composed of a rough and a turbo pump) while the other end is connected to an Ar gas tank. A diagram of the setup can be seen in the figure below.
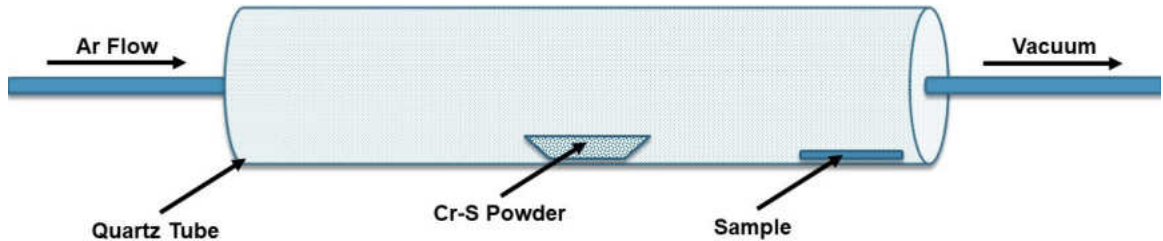


Figure 6: Solid-vapor deposition diagram.

Later, the tube was pumped until the internal pressure reached $\sim 10^{-5}$ Torr and both ends were sealed with valves at both ends. Then, the tube was put in the furnace that was preheated to 500 °C. After heating the tube for 24 hours, the temperature was increased to 800 °C. The tube was heated at that temperature for 4 days. At the end, we used solid-vapor deposition method to deposit synthesized powder on sapphire samples. Whe temperature was increased to 850 °C and Ar gas was let to

flow for 30 minutes while the pressure was kept at $\sim 2$ Torr. Finally, Ar gas was cut while the pump was running and the tube was left to cool down slowly, about $4\,^{\circ}\mathrm{C}/\mathrm{min}$. Some of the powder was taken for XPS analysis and some for XRD analysis. The sapphire sample was taken for AFM imaging.

## 2.2 X-ray Photoelectron Spectroscopy

"To know XPS is to know the atom."

Dr. Paul van der Heide

### 2.2.1 Principles

One of the characterization techniques used in this project is x-ray photoelectron spectroscopy (XPS), or sometimes known as electron spectroscopy for chemical analysis (ESCA). This technique was developed in Sweden by Kai Siegbahn's research group in 1960s and brought Dr. Siegbahn a Nobel Prize in Physics in 1981 [6]. The main working principle is the photoelectric effect that was explained by Albert Einstein in 1905 who was awarded the Nobel Prize in Physics in 1921 for his works on this phenomenon [7]. In XPS, high energy x-ray photons are used to excite electrons of the substrate. The electrons ejected from the substrate are sorted out based on their kinetic energies with the help of hemi-spherical electron energy analyzer. In the last stage, the number of electrons with certain kinetic energies are directed to the electron detector and are counted. XPS software shows the number of electrons (N(E)) vs binding energy graphs. Although x-rays penetrate deep inside a sample, the photoelectrons have limited mean free path. Therefore, XPS is very surface sensitive [6, 8]. The binding energies of electrons are calculated using Equation 2.2.

$$E_{\text{initial}} = E_{\text{final}}$$

$$h\nu = KE + BE + \phi \tag{2.2}$$

where $h\nu$ is the energy of the photon, BE is the binding energy of the orbital from which the electron originates, KE is the kinetic energy of photoelectron and $\phi$ is the work function of the analyzer.

Each element has a unique set of binding energies; therefore, XPS can be used to identify and calculate the concentration of the elements in the surface. Changes in the binding energies come from the changes in local chemical environment of the electrons. The changes are used to identify the chemical state of the materials being studied [6]. Main components of an XPS system and the photoelectric effect are shown in the Figure 7.
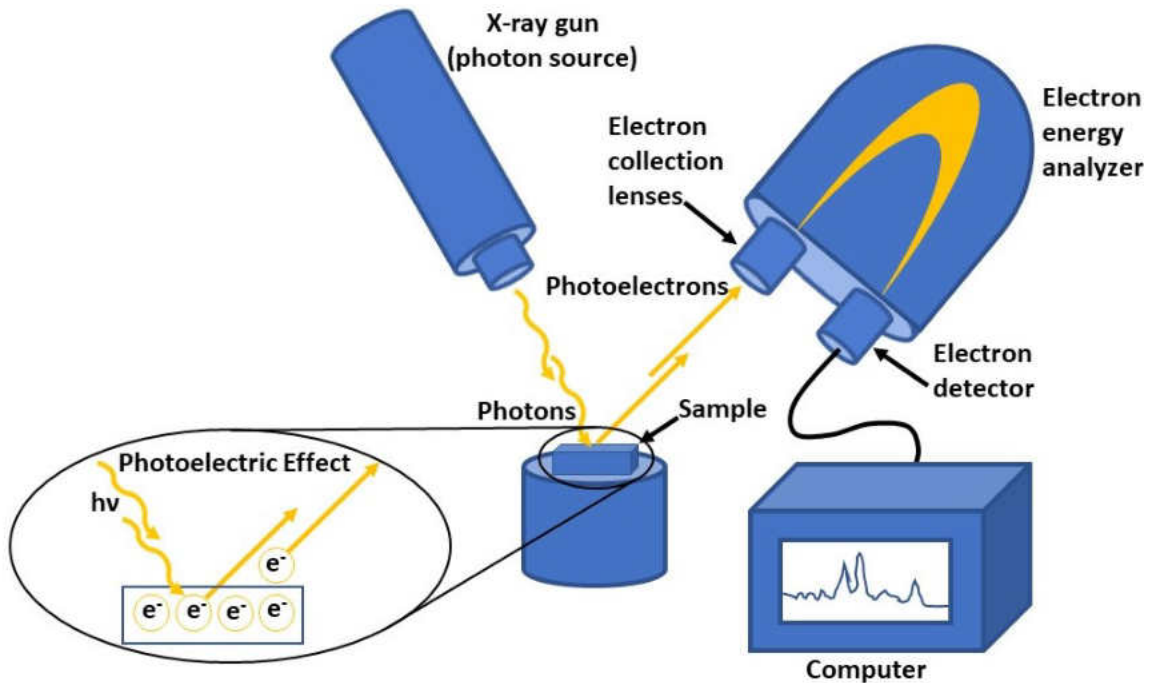


Figure 7: Diagram and main components of an XPS system.

## 2.2.2   Instrument

For this project, Perkin-Elmer brand PHI Model 5400 MultiTechnique system was used. This machine includes an ion gun for sputtering purposes as well. The system has a Model 10-550 x-ray source mounted with a Model 04-548 dual anode source. For this project, only Al K$\alpha$ (1486.6 eV) x-rays are used while the x-ray gun was powered at 300 W, 15 kV and 21 mA. The hemi-spherical analyzer is a Model 10-360 Electron Energy Analyzer with Omni-Focus III lens placed with 54° angle difference to the x-ray source [8]. All scans were taken under ultra-high vacuum (UHV) condition. The base pressure of the system is $\sim 10^{-10}$ Torr. A picture of the system can be seen in Figure 8.



Figure 8: Picture of the XPS system used in this project.

## 2.2.3   Data Acquisition

The software used for data acquisition and interpretation is AugerScan Version 3.3 by RBD Instruments, Incorporated. With this software, before each measurement, the signal intensity was optimized by adjusting the stage pos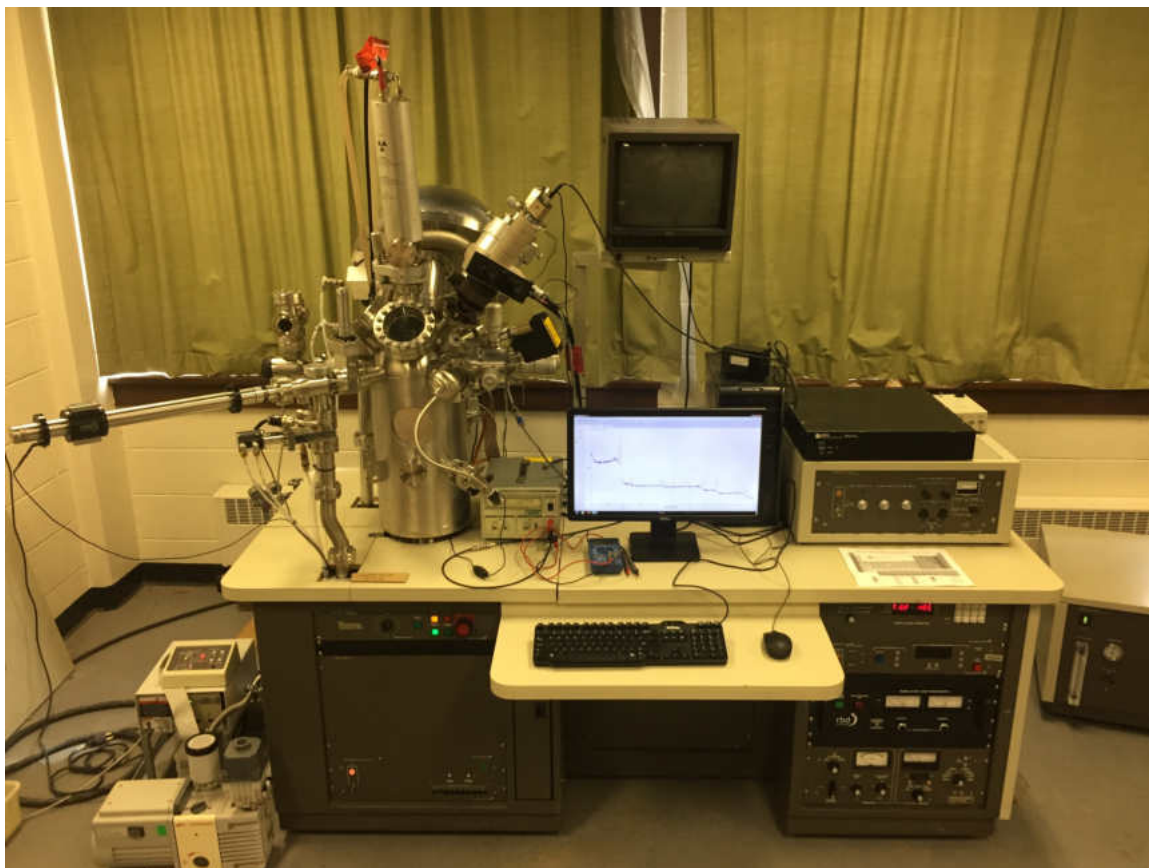ition. Survey and multiplex scans were performed for characterization. A survey scan gives a general information about the composition of the sample and the atomic concentration percentages of the present elements. A survey scan is usually done with larger energy steps and higher pass energies. Besides the main photoelectron peaks, there are also Auger peaks and satellite. On the other hand, multiplex is a measurement type that uses smaller pass energy and smaller step size in energy value. Pass energy limits the number of electrons permitted to reach the detector. A multiplex measurement provides a more precise and detailed information and can be focused on specific peaks [8]. Multiplex scans are used to obtain detailed chemical information about the elements being investigated.

## 2.2.4   Data Interpretation

In this subsection, Auger peaks, spin-orbit splittings, and multiplets, which were mentioned in the previous subsection, will be explained. Auger process is a result of a series of internal relaxation events. When a core shell electron is emitted, a hole forms. The atom becomes unstable and an outer shell electron fills the hole. The excess energy out of this process is transferred to a second outer shell electron. This second electron will be emitted if the transferred energy is greater than the binding energy. A diagram of this process can be seen in Figure 9.
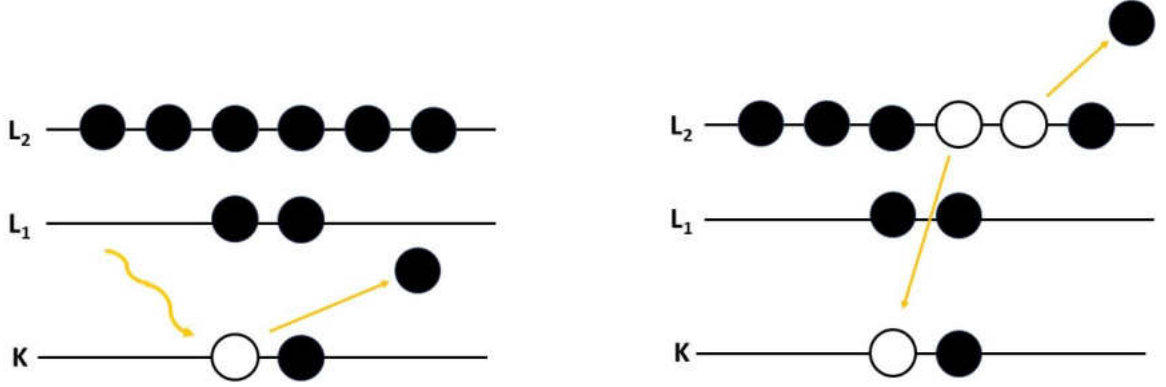
Figure 9: Diagram of a KLL Auger excitation.

Electromagnetic interaction between the electron's magnetic dipole moment and its orbital motion around positively charged nucleus form the basis of spin–orbit coupling [9]. Due to this effect, electrons' atomic energy levels shift. This phenomenon causes a detectable splitting of spectral lines. In the rest frame of the electron, the rotation of the proton around the electron generates a current which produces a magnetic field. With the help of Biot-Savart law,

$$\vec{B} = \frac{-Ze\vec{v} \times \vec{r}}{cr^3} \tag{2.3}$$

this magnetic field couples to electron's intrinsic spin magnetic moment via the following Hamiltonian,

$$\hat{H} = -\vec{\mu} \cdot \vec{B} = \left(-\frac{ge}{2m_ec}\vec{S} \cdot \frac{-Ze\vec{v} \times \vec{r}}{cr^3}\right) = \frac{Ze^2}{m_e^2c^2r^3}\vec{S} \cdot \vec{L}. \tag{2.4}$$

Equation 2.4 indicates that for orbitals with non-zero orbital angular momentum (i.e. p, d and f), there will be always a spin-orbit splitting due to spin-orbit coupling.

On the other hand, multiplet splitting is due to the coupling of unpaired electrons. Photoionization creates an electron vacancy in one of the core levels. The coupling between this unpaired electron in the core and the unpaired electrons in the outer

11

shell leads to several final states, which will show itself in the photoelectron spectrum as a multi-peak envelope [6, 8]. This phenomena is common to the first-row transition metals where the atoms have unpaired electrons in the $d$ shell, e.g., Cr(+3): [Ar] $3d^3$. Figure 10 shows this phenomenon.
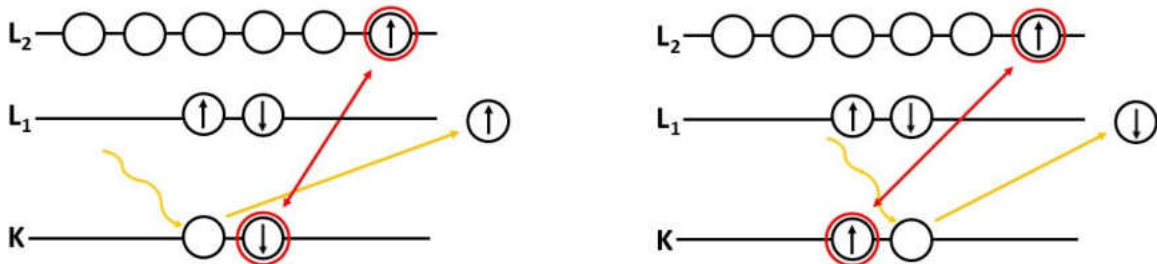


Figure 10: Unparied electrons from the core shell and outer shell, circled in red, cause the multiplet splitting.

## 2.3   X-ray Powder Diffraction

X-ray powder diffraction (XRD) is a powerful characterization method for phase identification of a crystalline material and can provide information on dimensions of unit cell. X-rays are generated by a cathode ray tube, then they are filtered to produce monochromatic radiation. X-ray waves are scattered primarily through the atoms' electrons. In a crystal, atoms are arranged in a highly ordered structure. X-ray waves elastically scattered by the atoms of a crystal produces a regular array of spherical waves. Scattered X-ray waves interfere constructively and destructively. Due to destructive interference, in most directions these waves cancel out, however in a few specific directions determined by Bragg's law, they add up constructively [10]. Bragg's law is defined by Equation 2.5.

$$2d \sin \theta = m\lambda \tag{2.5}$$

where $d$, $\lambda$ and $\theta$ are interplanar spacing, the wavelength of the X-ray and angle of incidence, respectively. $m$ is a dimensionless integer.
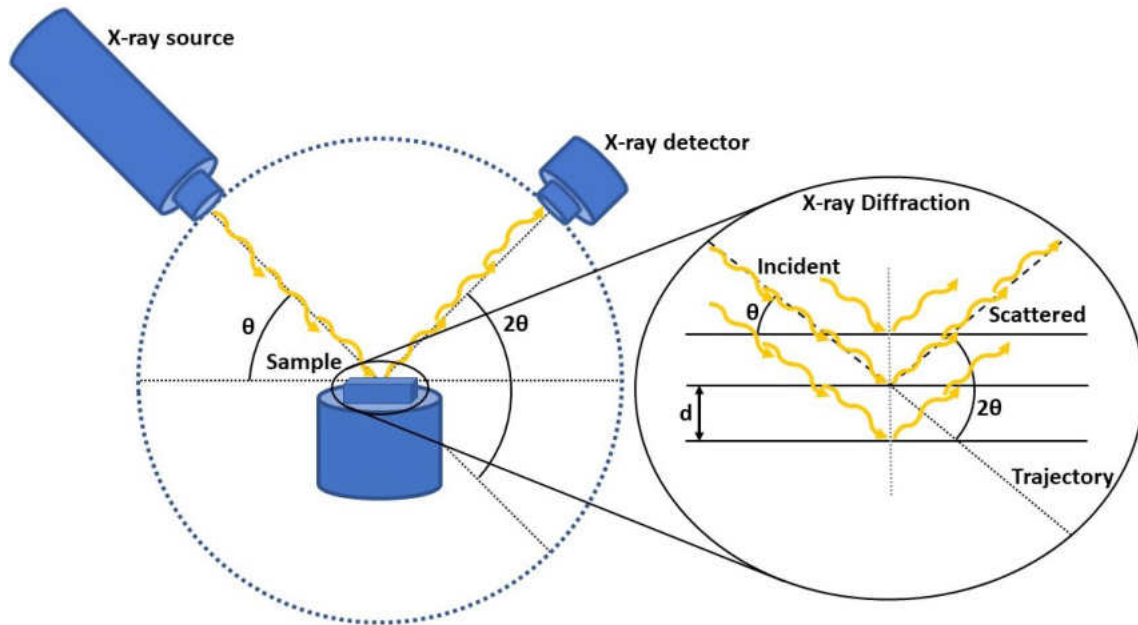
Figure 11: Diagram of an XRD system.

XRD measurements were conducted in the Chemical Engineering Department at the University of North Dakota by Dr. Xiadong Hou. A Rigaku Smartlab Diffractometer was used. As the source, Cu K$\alpha$ was used with 40 kV voltage and 44 mA current. D/TEX detector was used in the 2$\theta$ range with 0.02° steps at 2°/min speed.

## 2.4 Atomic Force Microscopy

Atomic force microscopy (AFM) is a technique to obtain topographical images. A typical AFM has a laser, a photodiode, a cantilever, and a controller as main components. An AFM can operate in three imaging modes, contact mode, tapping mode and non-contact mode. In this project, we used tapping mode. In tapping mode, the cantilever is driven to oscillate at or near its resonance frequency. The frequency and amplitude of the driving signal are kept constant. As the tip at end of the cantilever scans the surface, the interaction between the tip and the surface cause the amplitude of the cantilever's oscillation to change (usually decrease). This amplitude is used as a parameter to control the height of the cantilever above the sample. The

13

electronics adjust the height of the cantilever to maintain a fixed oscillation amplitude during a scan. Therefore, a tapping AFM image is a result of the intermittent contacts of the tip with the sample surface [11]. Below is a diagram of an AFM.
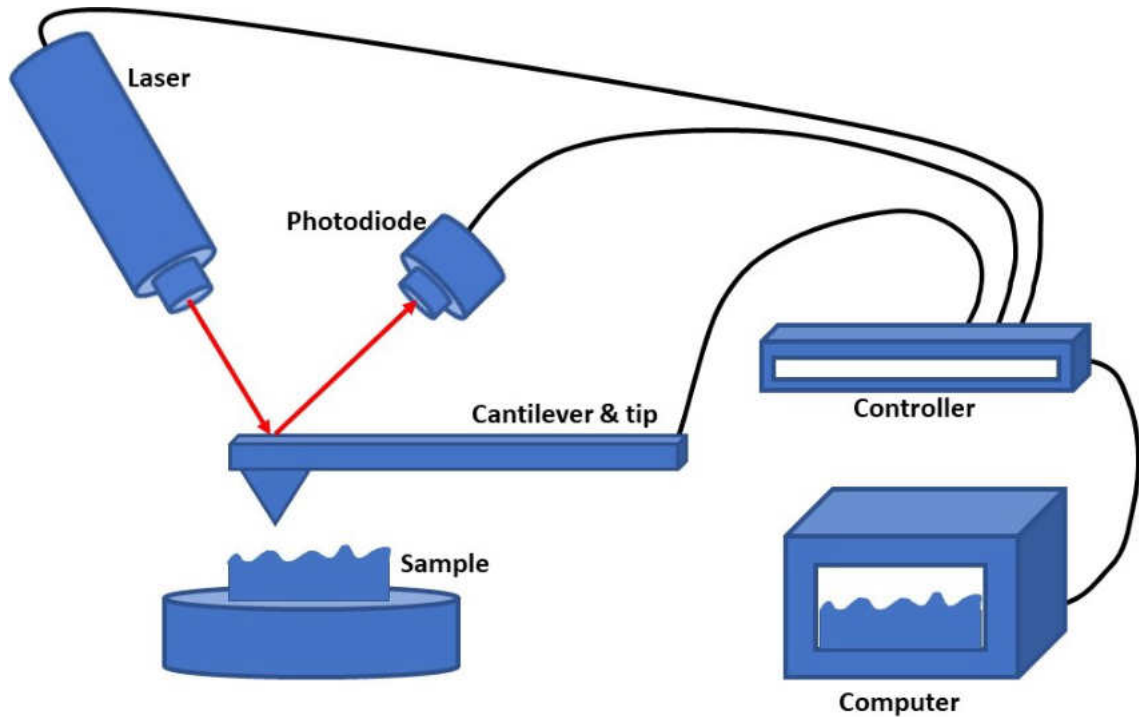


Figure 12: Diagram of an AFM.

For this project, Nanomagnetics Instruments brand, ezAFM system with Nanosensors Aspire Conical non-contact (tapping mode) tips (Part Number: CT170R-10) were used. These tips have 50 N/m spring constant and 170 kHz resonance frequency. They are coated with Al and the radius of curvature of the tip is 8 nm as reported by the product data sheet [12]. Data is acquired with the ezAFM's own software. However, the data analysis was conducted with Gwyddion, a free scanning probe microscopy software.

# CHAPTER III

# RESULTS

As mentioned in detail in the methodology chapter, at the end of a 5-day long synthesis and slowly cooling down to room temperature, both the powder and the sapphire substrate were taken out of the reaction vessel. Synthesized powder was split into two for XPS and XRD analyses. The sapphire substrate with the synthesized powder was taken for AFM imaging.

It is beneficial to report here that the air leakage during the synthesis or deposition stages causes different results. As will be discussed later, at some point this issue was resolved and synthesis of 99.13% pure $Cr_2S_3$ was achieved.

For the reason mentioned above, from now on sample synthesized on 7 September 2018 will be referred as Sample A and the one synthesized on 14 February 2019 with 99.13% purity will be referred as Sample B. Different characterization techniques results will be provided and discussed separately for these two samples in this chapter.

## 3.1   Sample A

### 3.1.1   XRD Results

According to XRD analysis, Sample A contains two different compounds of chromium sulfides; $Cr_2S_3$ and $Cr_3S_4$ (Brezinaite) and also $Cr_2O_3$ (Eskolaite). Below is the XRD result.
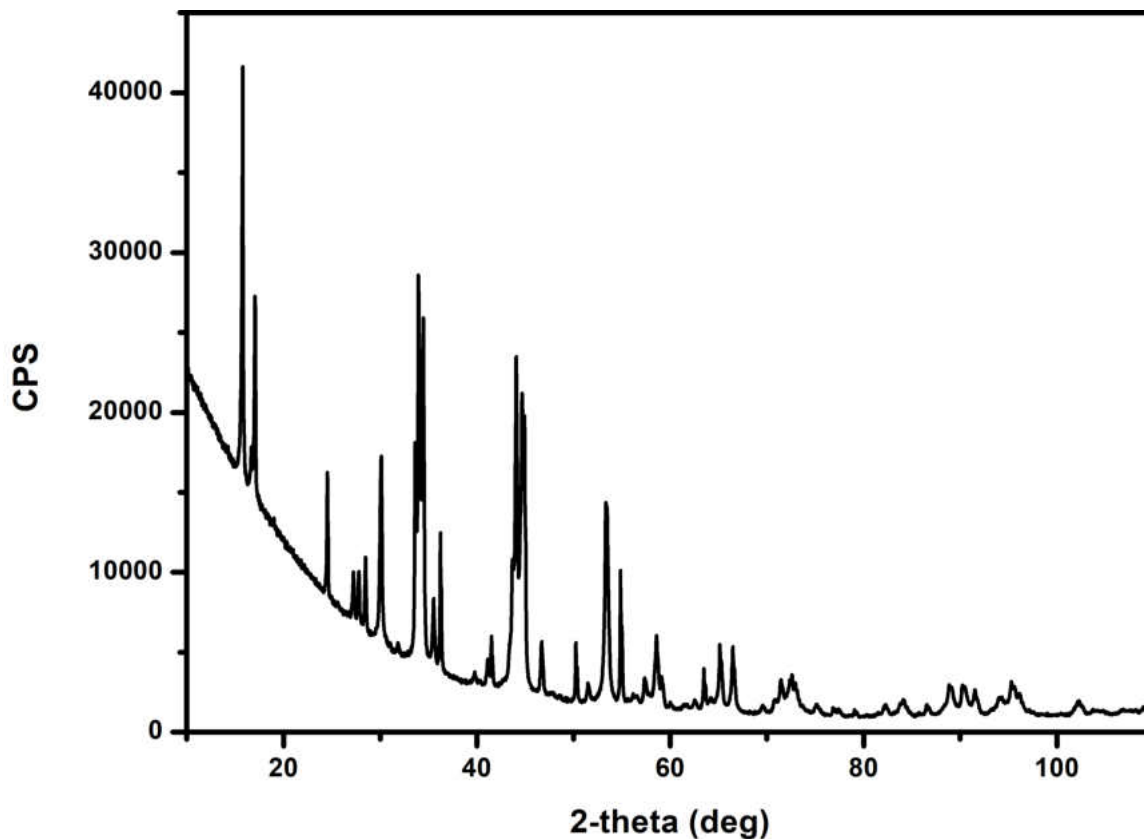
Figure 13: XRD result of Sample A.

Weight ratio of the before mentioned compounds according to this result is given in the below table.

Table 1: Content percentage of Sample A.

| Compound | Content (%) |
|----------|-------------|
| $Cr_3S_4$ | 64.5 |
| $Cr_2S_3$ | 13.2 |
| $Cr_2O_3$ | 22.3 |

## 3.1.2 XPS Results

For the survey, 89.45 eV pass energy, 0.5 eV/step, 50 msec/step and 4.65 eV work function were used, and 5 sweeps were taken.
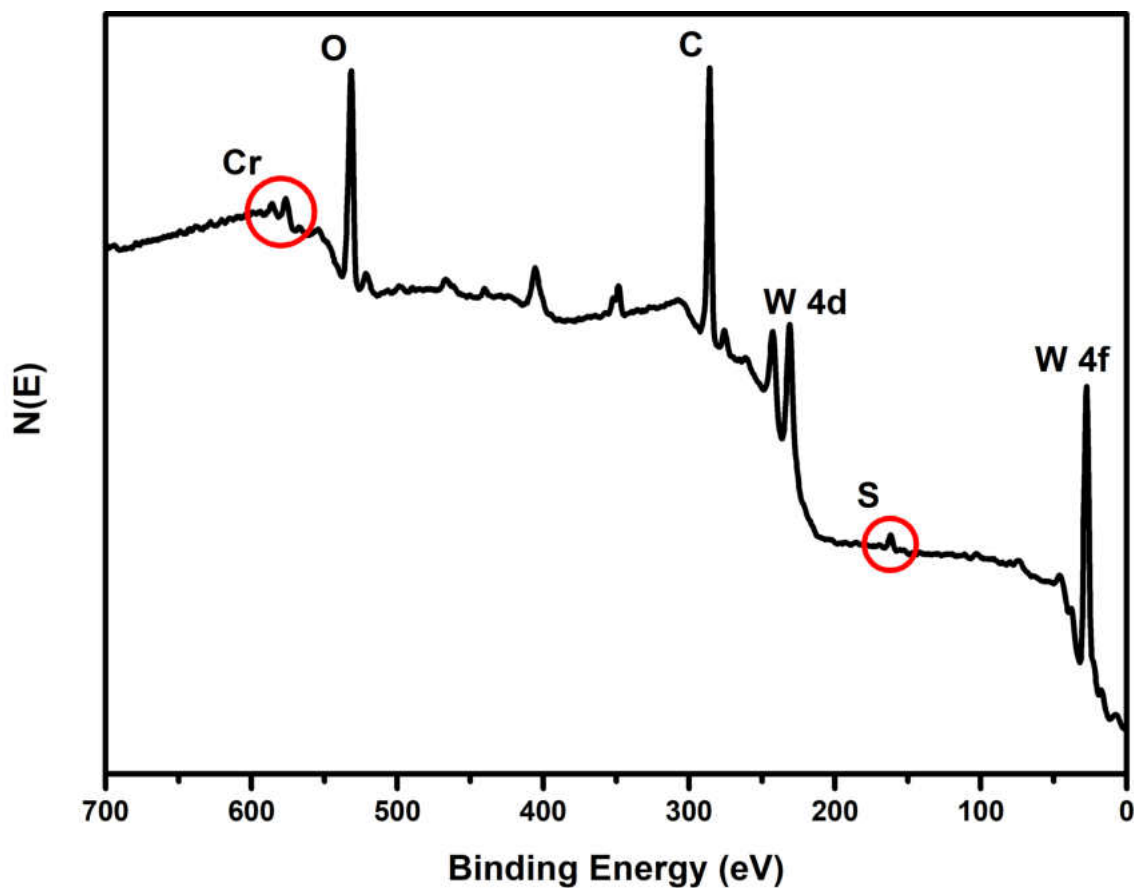
Figure 14: XPS survey scan result of Sample A.

It can be seen in the survey that both chromium and sulfur present in the sample. Along with them, oxygen, carbon and tungsten are seen. Tungsten peak is coming from the tungsten sheet being used as a substrate to hold the powder.

For the multiplex study, 17.9 eV pass energy, 0.025 eV/step, 50 msec/step and 4.65 eV work function were used and 20 sweeps were taken. These sensitive settings, when compared to those of survey scan given above, will provide more precise results.
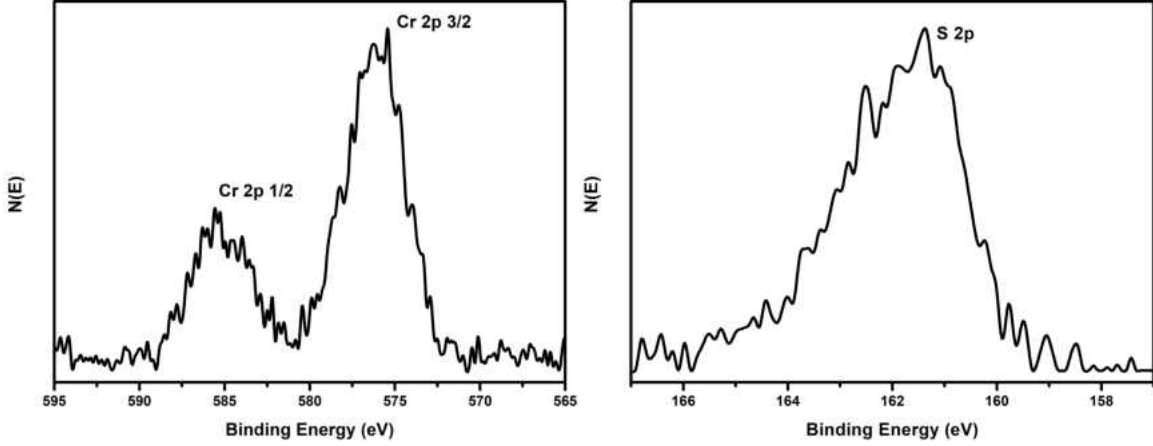
Figure 15: Multiplex measurement results of Sample A.

Since this sample is a multi-phase sample, it is extremely difficult to conclude the content of this sample with XPS analysis. Therefore, fittings of these multiplex will not be presented here. Elemental chromium 2p 3/2 and sulfur 2p have peak values at 574 eV and 164 eV respectively. For sample A, chromium peaks move to higher binding energies. Chromium 2p 3/2 peak was measured at 576 eV which is closer to the chromium peak measured in chromium oxide (576.9 eV). Since sulfur is less electronegative than oxygen, it is expected that the shift in binding energy of chromium electrons should be less. On the other hand, in comparison to elemental sulfur, sulfur 2p peak in sample A shifted to a lower binding energy of 161.5 eV which is in line with the literature [8].

### 3.1.3   AFM Images

Below are the AFM images of Sample A, deposited on clean sapphire substrates. Surface structure of the sapphire can be seen as well.
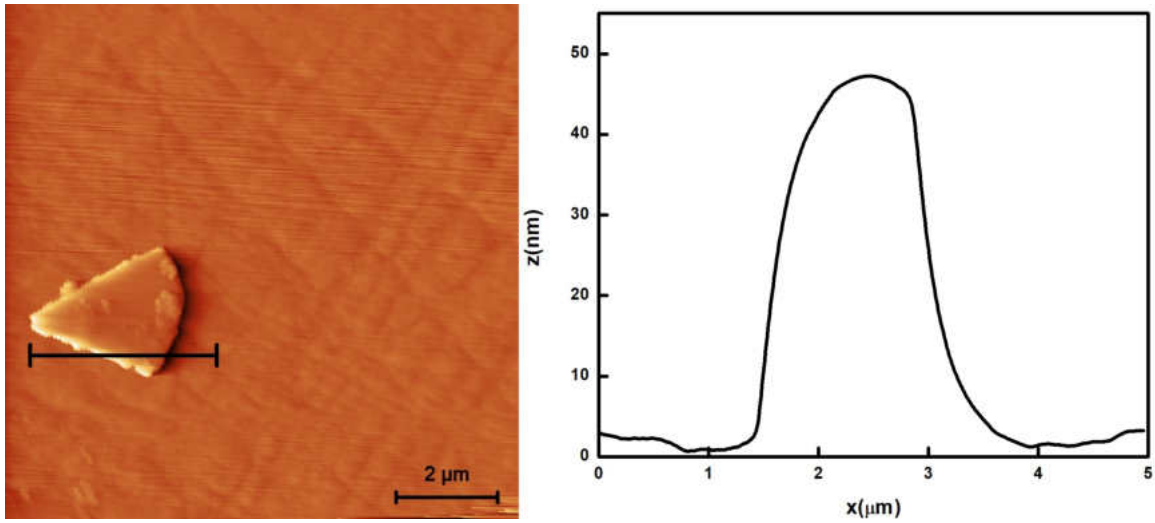
Figure 16: An AFM image of a particle and its height profile.

As can be seen above, triangular–shaped chromium sulfides were managed to be synthesized and deposited on sapphire substrate. These particles have approximately $3 \ \mu m^2$ of area size and according to the height profile particle in the above figure is about 45 nm thick. According to the crystal structure information given in introduction Chapter I and a published work, these particles are $Cr_2S_3$ [13]. It is calculated by taking the single unit cell height as 1.6 nm that the deposited particle is about 30 unit cells.



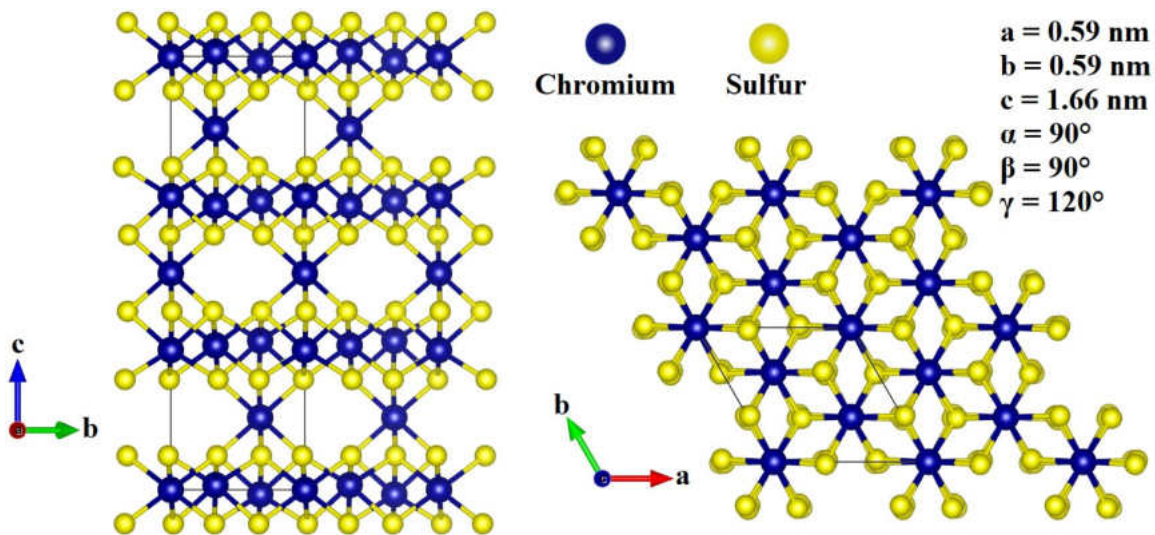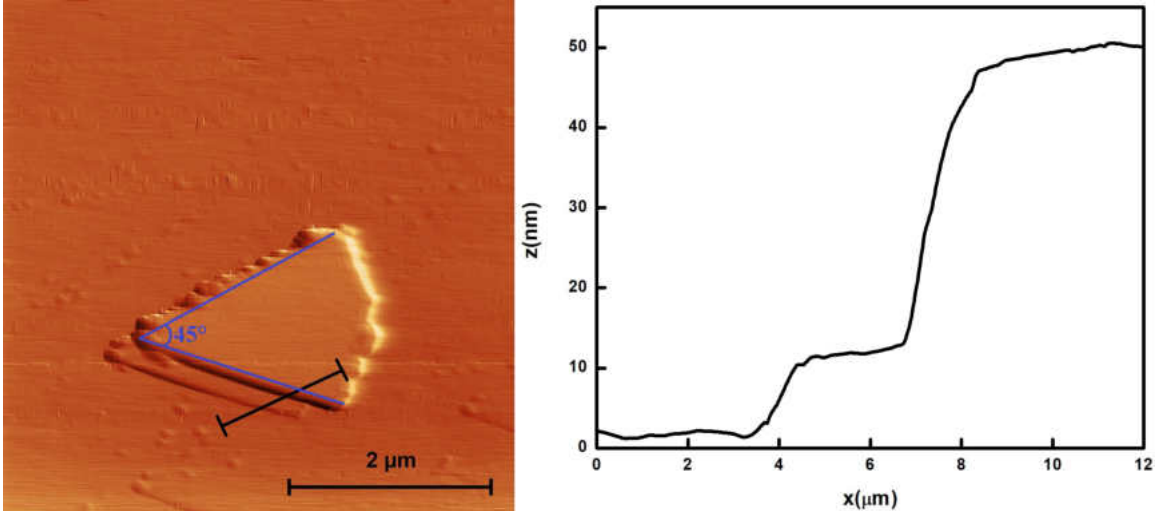Figure 17: Crystal structure of rhombohedral $Cr_2S_3$ and its parameters.

Figure 18: Another AFM image and a height profile.

As can be seen in the above image, particles can land on each other. In this particular case we were able to see the bottom layer and measure its height as $\sim 10$ nm which corresponds to 6 unit cells. This is the smallest layer number we have managed to image. Also in Figure 18, the characteristic angle for these isosceles triangles is identified as 45°.

## 3.2 Sample B

After observing Sample A, we shifted our objective to synthesize $Cr_2S_3$ with higher purity. We have tried different techniques and had many other sample in between samples A and B. Some of these were successful; some were not. However, here we are not going to discuss the trials but rather will focus on the end-product Sample B with 99.13% purity. This allows us to study XPS in depth that we skipped for Sample A in this work.

The difference of making this sample is that instead of using metal couplings on both ends of the fused-quartz tube, we sealed both ends of the tube by melting them with an oxyacetylene torch. Because synthesis needs to be done in an air-free environment, we sealed one end while vacuuming it. When the sealing was complete,

20

the internal pressure was $\sim 5 \times 10^{-4}$ Torr. The rest of the procedure was the same as Sample A which was described in the Chapter II.

### 3.2.1   XRD Results

Figure 19 shows the XRD result. Red line is showing the calculated $Cr_2S_3$ data. The difference between that and the measured data is due to the elemental chromium. When the ratios were compared, this gave us 99.13% $Cr_2S_3$.
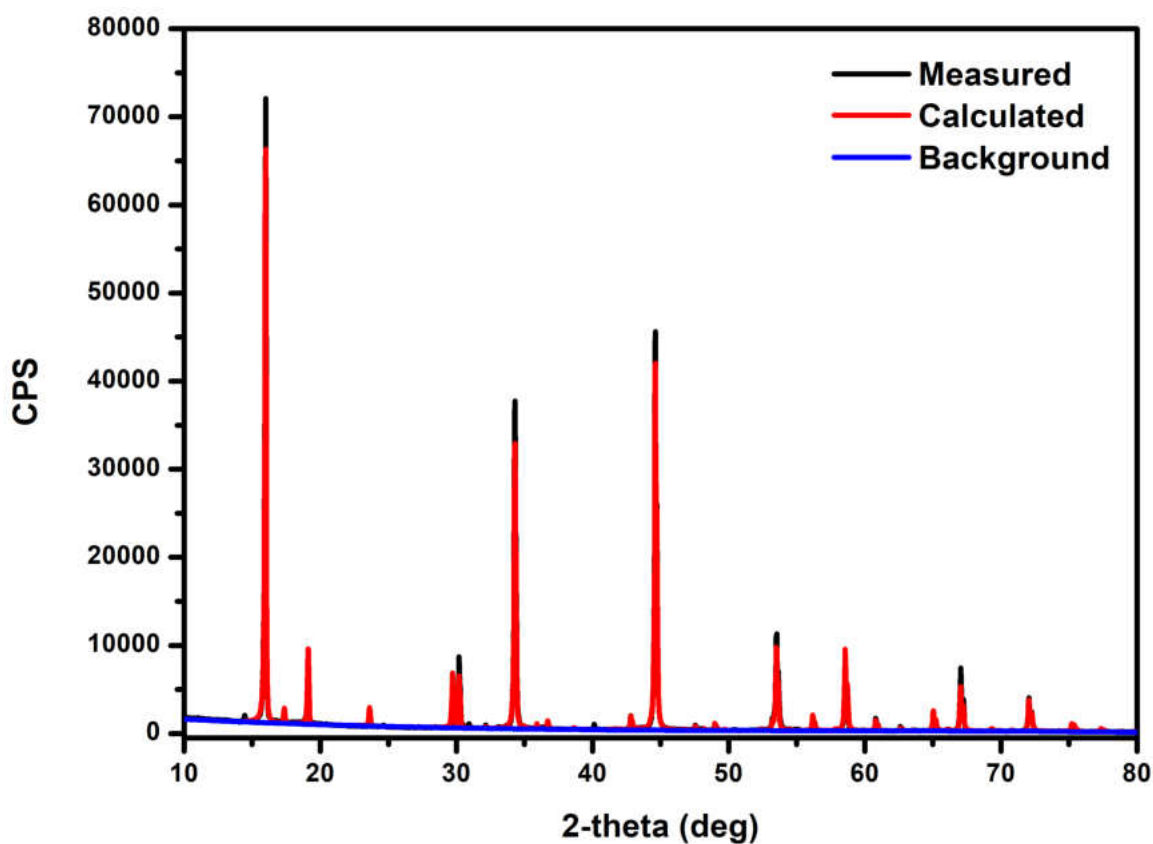


Figure 19: XRD result of Sample B.

Here, the difference between the measured and the calculated data is very small. Calculated data contains only $Cr_2S_3$ and Cr metal. Table 2 below shows the weight ratio of these two.

Table 2: Content percentage of Sample B.

| Compound | Content (%) |
|----------|-------------|
| Cr | 0.87 |
| $Cr_2S_3$ | 99.13 |

### 3.2.2 XPS Results

At the end of the synthesis, we had a big chunk of $Cr_2S_3$ as well as some powder. We used the chunk for XPS analysis. Below is the XPS survey result of this sample,
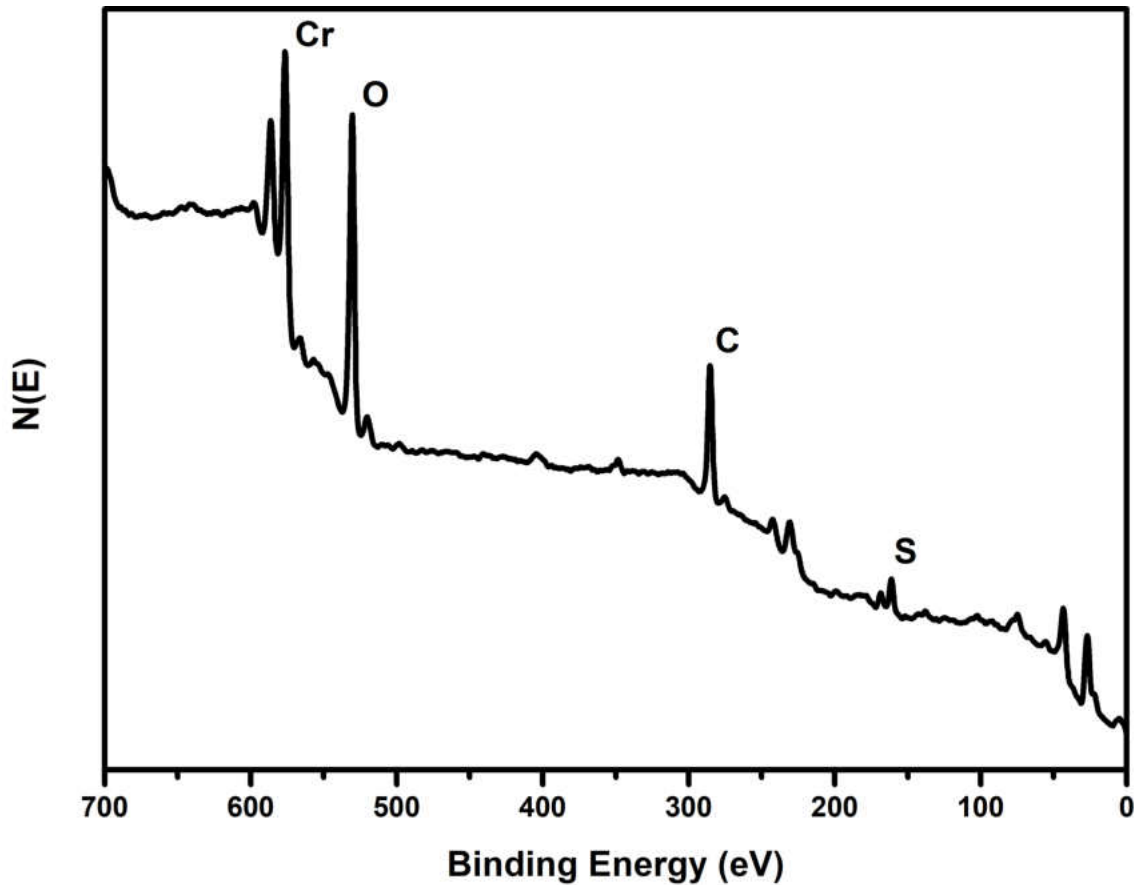


Figure 20: XPS survey scan result of oxidized Sample B surface.

As it can be seen in the survey, there is some oxygen and carbon on the sample. This result seems to contradict with the XRD data which did not indicate any oxide or carbide formation. The discrepancy between XPS and XRD data can make sense only if the oxygen and carbon contamination is just on the surface. In order to solve

this puzzle, we sputter–cleaned the sample surface. The sample was sputtered with $Ar^+$ ions generated at 5 kV beam voltage and 25 mA emission current for 15 minutes. Survey after the sputtering can be seen below.
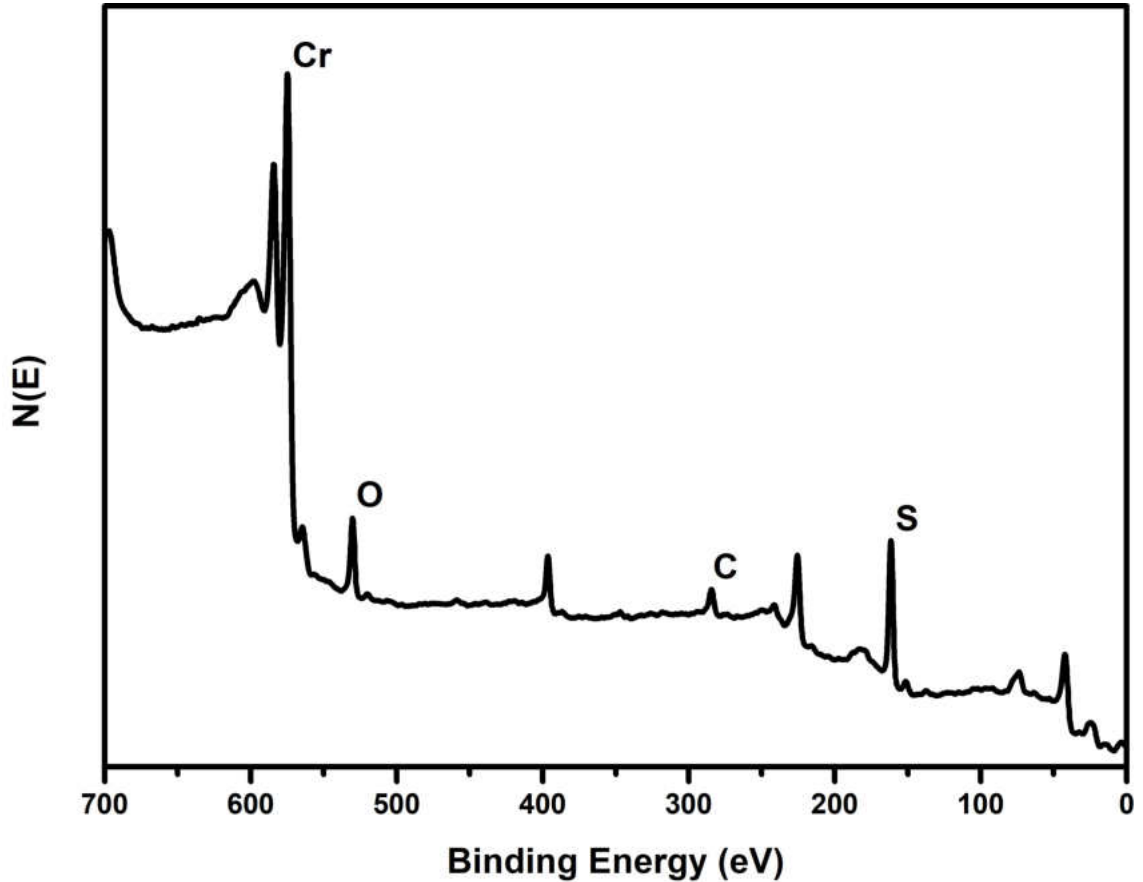


Figure 21: XPS survey scan result of Sample B after sputter-etching the surface.

Comparing this graph to Figure 20, we immediately notice a big drop at oxygen and carbon peaks relative to chromium and sulfur peaks. This confirmed our prediction that the contamination was just on the surface.
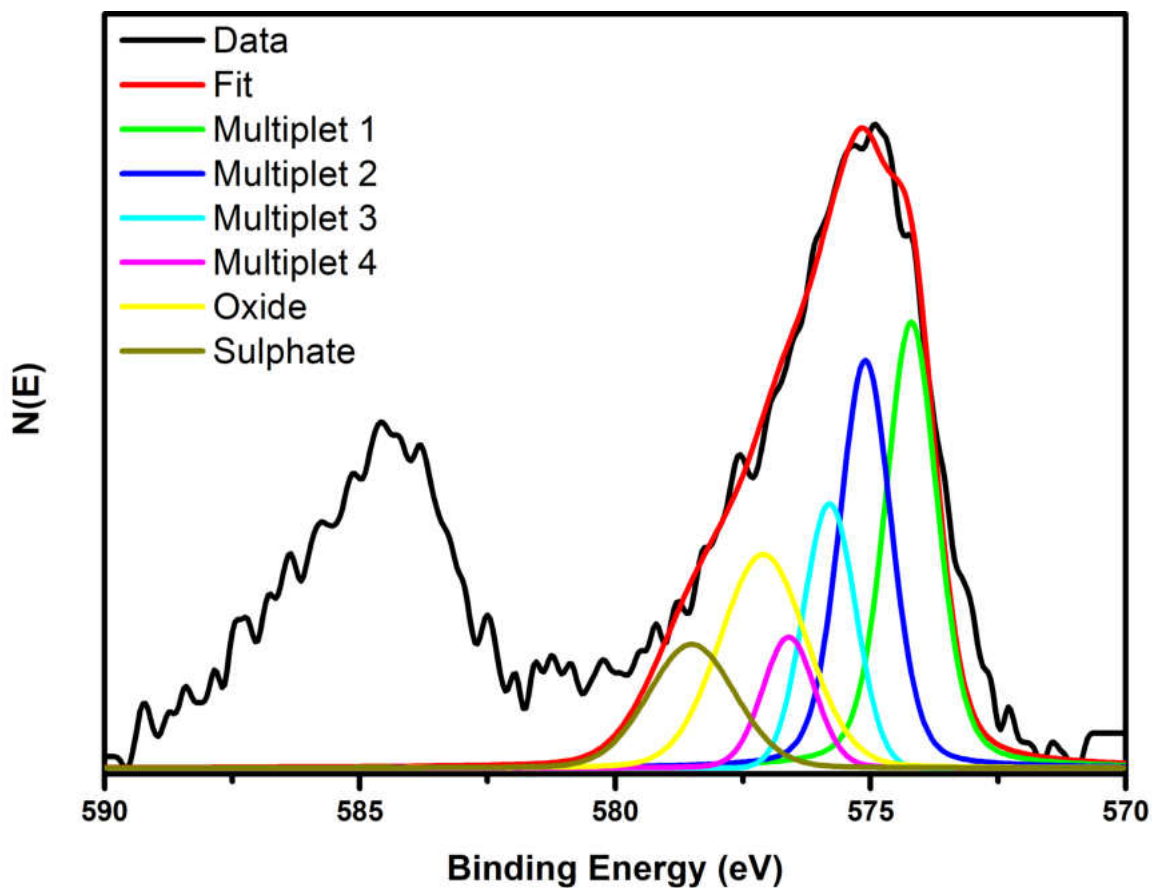
Figure 22: Cr 2p multiplex measurement result of Sample B.

Above is the chromium 2p multiplex scan. Here we observe a spin-orbit splitting, which was described in the methodology chapter. The peak on the right is 2p 1/2 and the one on the right is 2p 3/2. In order to understand the composition, we needed to fit 2p 3/2 peak with 4 multiplets and 2 other possible peaks. We compared our results with what was reported before in terms of the positions, full-width at half-maximum (FWHM) values and area percentages of fitted peaks [14]. Below is the table showing our fitting parameters versus the reported values.

Table 3: Comparison of measured and reported values of Cr 2p multiplets.

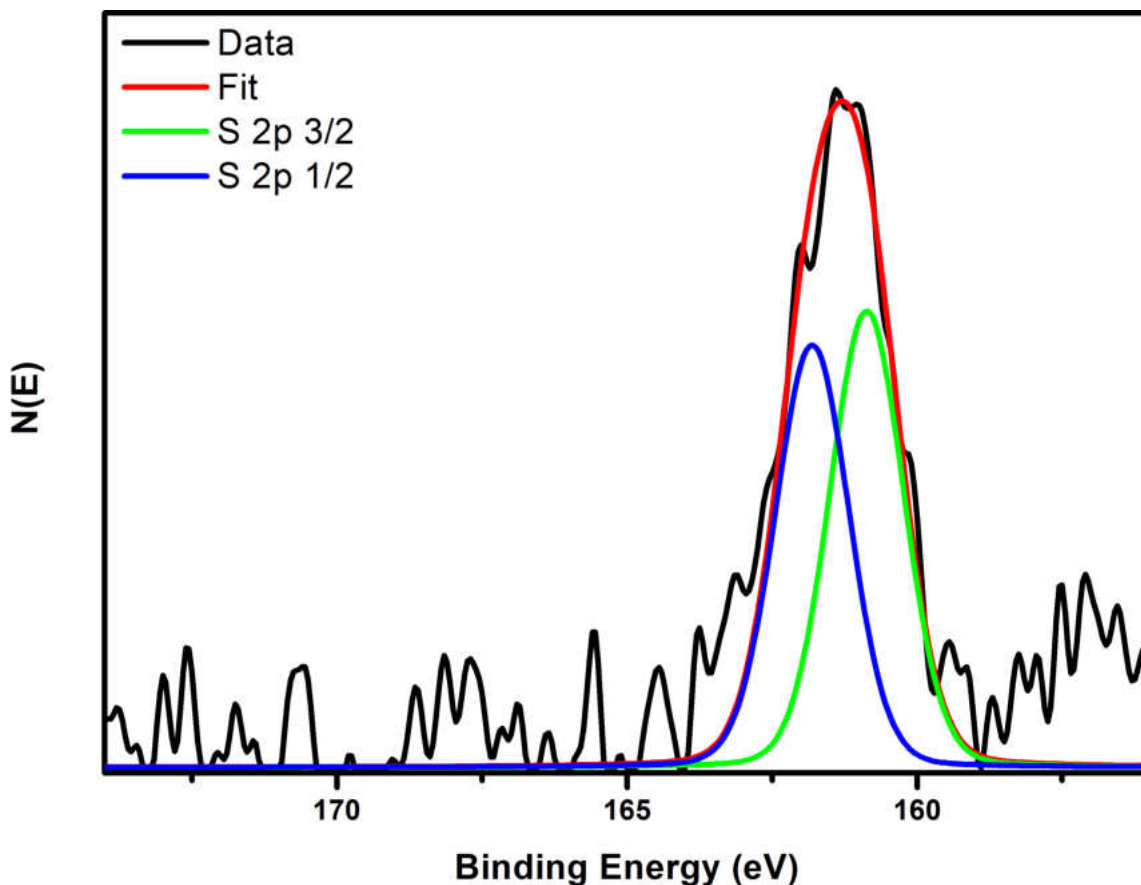| Name | Measured Position | Measured FWHM | Measured % Area | Reported Position | Reported FWHM | Reported % Area |
|---|---|---|---|---|---|---|
| Multiplet 1 | 574.2 | 1.2 | 26.2 | 574.2 | 0.91 | 33.3 |
| Multiplet 2 | 575.1 | 1.2 | 23.3 | 575.1 | 0.91 | 27.3 |
| Multiplet 3 | 575.8 | 1.2 | 13.5 | 575.8 | 0.91 | 14.4 |
| Multiplet 4 | 576.6 | 1.2 | 7.0 | 576.6 | 0.91 | 3.1 |
| Oxide | 577.1 | 2.0 | 19.0 | 577.1 | 2.0 | 13.7 |
| Sulphate | 578.5 | 2.0 | 11.0 | 578.5 | 2.0 | 8.3 |



Figure 23: S 2p multiplex measurement result of Sample B.

Above is S 2p peak and its fitting. We used spin-orbit split pair to fit the experimental data. As expected, S 2p 3/2 peak is at 160.9 eV which is shifted to a lower binding energy than that of elemental sulfur [8].
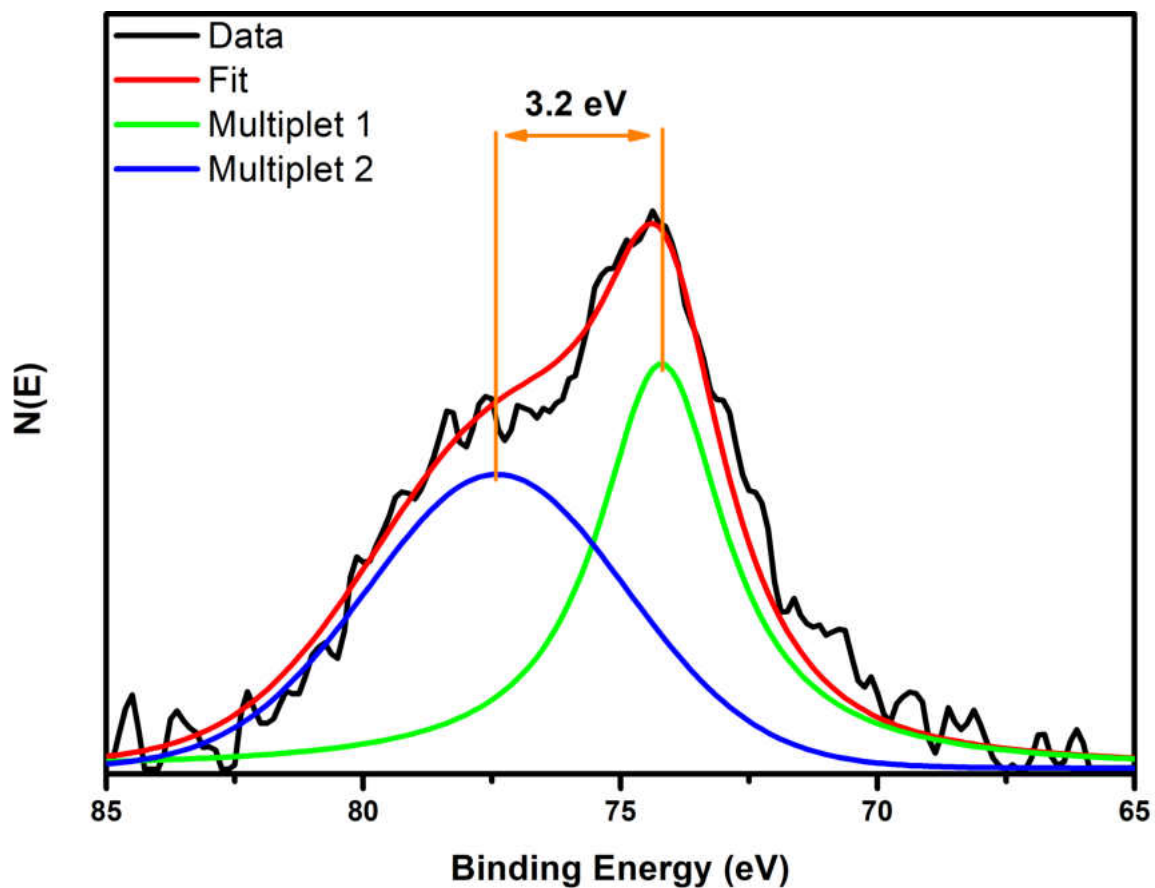
Figure 24: Cr 3s multiplex measurement result of Sample B.

Above is the chromium 3s peak and because the orbital angular momentum value ($l$) is zero, we do not observe a spin-orbit splitting here. However, we observed multiplet splitting. The multiplet pair separated by 3.2 eV. Which matches the previously reported data [15].

# CHAPTER IV

# CONCLUSION

Transition metal chalcogenides (TMC) are made from transition metal and chalcogen atoms with the general formula of $M_nX_m$. They exhibit a wide range of electrical, magnetic and chemical properties [2]. Recently, transition metal dichalcogenides have gained popularity due to their two-dimensional nature which in return has rejuvenated the traditional methods to synthesize TMCs. Motivated by the novel properties of these materials, we decided to study chromium sulfides, in particular $Cr_2S_3$. Bulk $Cr_2S_3$ have been studied before because of its magnetic properties. However, physical and chemical properties of nano-scale particles have never been investigated. We followed the $Cr_2S_3$ synthesis reported in Vaqueiro et al.'s paper [4]. We synthesized $Cr_2S_3$ with 99.13% purity in quartz tubes sealed with oxyacetylene torch. The quality of the synthesized materials were studied with XRD and XPS techniques. We used vapor-solid growth method to deposit synthesized materials on sapphire substrates. AFM images of these samples confirmed quasi-2D nature of the material.

# REFERENCES

[1] Novoselov, K. et al. Electric Field Effect in Atomically Thin Carbon Films. Science 306, 666-669 (2004).

[2] Choi, W. et al. Recent development of two-dimensional transition metal dichalcogenides and their applications. Materials Today 20, 116-130 (2017).

[3] Jellinek, F. The structures of the chromium sulphides. Acta Crystallographica 10, 620-628 (1957).

[4] Vaqueiro, P. et al. Colossal magnetoresistance in the layered chromium sulfide $Cr_2S_{3-x}$ ($x = 0.08$). Physical Review B 64, (2001).

[5] mp-849083: Cr2S3 (trigonal, P3, 143). Materialsproject.org (2019). at `https://materialsproject.org/materials/mp-849083/`

[6] Van der Heide, P. X-ray Photoelectron Spectroscopy. (Wiley, 2011).

[7] Einstein, A. Über einen die Erzeugung und Verwandlung des Lichtes betreffenden heuristischen Gesichtspunkt. Annalen der Physik 322, 132-148 (1905).

[8] Wagner, C. & Muilenberg, G. Handbook of x-ray photoelectron spectroscopy. (Physical Electronics Division, Perkin-Elmer Corp., 1979).

[9] Sakurai, J. & Napolitano, J. Modern quantum mechanic. (Addison-Wesley, 2011).

[10] Poppe, L. A laboratory manual for x-ray powder diffraction. (U.S. Geological Survey, Coastal and Marine Geology Program, 2001).

[11] Meyer, E., Hug, H. & Bennewitz, R. Scanning probe microscopy. (Springer, 2004).

[12] Nanoscience Instruments, Aspire CT170. `https://store.nanoscience.com/aspire-ct170.html`

[13] Chu, J. et al. Sub-millimeter-Scale Growth of One-Unit-Cell-Thick Ferrimagnetic Cr2S3 Nanosheets. Nano Letters 19, 2154-2161 (2019).

[14] Biesinger, M., Brown, C., Mycroft, J., Davidson, R. & McIntyre, N. X-ray photoelectron spectroscopy studies of chromium compounds. Surface and Interface Analysis 36, 1550-1563 (2004).

[15] Carver, J., Schweitzer, G. & Carlson, T. Use of X-Ray Photoelectron Spectroscopy to Study Bonding in Cr, Mn, Fe, and Co Compounds. The Journal of Chemical Physics 57, 973-982 (1972).

[16] Kittel, C. Introduction to solid state physics. (Wiley, 2005).

[17] Hofmann, S. Auger- and X-Ray Photoelectron Spectroscopy in Materials Science. (Springer Berlin Heidelberg, 2013).

[18] Luth, H. Solid Surfaces, Interfaces and Thin Films. (Springer Berlin Heidelberg, 2010).